Journal of Quantitative Spectroscopy & Radiative Transfer 360 (2026) 109940

Contents lists available at ScienceDirect

Journal of Quantitative Spectroscopy and Radiative Transfer

journal homepage: www.elsevier.com/locate/jqsrt

Capability of liquid cloud microphysical property retrieval from satellite-borne multi-angle hyperspectral polarimetric measurements☆

Zihao Yuan [a,b,*], Bastiaan van Diedenhoven [a], Guangliang Fu [a], Hai Xiang Lin [b,c], Jan Willem Erisman [b], Otto P. Hasekamp [a]

[a] SRON Netherlands Institute for Space Research (NWO-I/SRON), Niels Bohrweg 4, Leiden, 2333 CA, South Holland, The Netherlands
[b] Institute of Environmental Science (CML), Leiden University, Einsteinweg 2, Leiden, 2333 CC, South Holland, The Netherlands
[c] Delft Institute of Applied Mathematics, Delft University of Technology, Mekelweg 4, Delft, 2628 CD, South Holland, The Netherlands

A R T I C L E I N F O

Keywords:
Cloud
Polarimetric retrieval
Neural network

A B S T R A C T

This paper assesses the capability of liquid cloud droplet effective radius (CER) and cloud effective variance (CEV) retrieval from space-borne multi-angular hyperspectral measurements. The capability and sensitivity study is based on a neural network (NN) retrieval approach which is developed for the Spectropolarimeter for Planetary EXploration - one (SPEXone), a multi-angular hyperspectral polarimeter onboard Plankton, Aerosol, Cloud, ocean Ecosystem (PACE) satellite. The synthetic measurements used in NN training and the sensitivity experiments are generated by Remote sensing of Trace gas and Aerosol Products (RemoTAP) forward model, and include variations of cloud, surface and aerosol properties, as well as cloud fraction. On the basic validation set, the NN performs similar over ocean and land with a mean absolute error (MAE) around 2 μm on CER and around 0.04 on CEV. The performance over different cloud fraction (CF) and cloud optical thickness (COT) is evaluated, and indicates that most accurate retrievals can be performed for cases where CF > 0.6 and COT between 2 and 12. The sensitivity to above-cloud aerosols (both fine-mode-dominated and dust-mode-dominated cases) suggests the retrieval is more sensitive to absorbing fine mode aerosols (CER MAE < 2.5 μm up to AOT of 0.2 for fully cloudy scene), than to dust aerosols (CER MAE < 2.5 μm up to AOT of 0.5). Moreover, the retrievals are virtually insensitive to above cloud cirrus over fully cloudy scene, but shows large sensitivity over partly cloudy scenes over land. Finally, synthetic measurements from partly cloudy scenes are generated based on the 3D MYSTIC radiative transfer model. The retrieval on these measurements suggests no significant 3D cloud radiative effect artifacts.

1. Introduction

Clouds are key regulators of Earth's climate because they both reflect incoming solar radiation (cooling effect) and trap outgoing infrared radiation (warming effect), directly influencing the planet's energy balance. The type, altitude, and structure of clouds determine whether their net effect is to cool or warm the planet. For example, low, thick clouds tend to cool by reflecting sunlight, while high, thin clouds tend to warm by trapping heat. However, clouds remain one of the largest sources of uncertainty in predicting climate change [1]. The uncertainty is both related to cloud feedback [2,3] as well as aerosol–cloud interactions (ACI) [4–6].

In quantification of aerosol–cloud interactions, global measurements of the cloud droplet size distributions are of crucial importance [7,8]. Satellite-borne remote sensing is the only practical way to acquire global information of cloud droplet effective radius (CER). The two MODIS (Moderate Resolution Imaging Spectroradiometer) instruments (onboard the Aqua and Terra satellites) provide various cloud data products for cloud microphysical property monitoring for more than 20 years. The MODIS CER retrieval algorithm employs the bi-spectral method [9], which uses a look-up table (LUT) of reflectances at a mid-visible wavelength and a shortwave infrared wavelength to obtain the CER and cloud optical thickness (COT) that best matches the observation [10]. This algorithm provides global, high-resolution, daytime retrievals of CER and COT, especially for optically thick, overcast, single-layer liquid clouds [11], and is also applied on other instruments like NOAA AVHRR [12] and VIIRS [13]. However, a limitation of bi-spectral retrievals from single-viewing instruments is degraded capability over broken cloud fields and large sensitivity

☆ This article is part of a Special issue entitled: 'APOLO-2024' published in Journal of Quantitative Spectroscopy and Radiative Transfer.

* Corresponding author at: SRON Netherlands Institute for Space Research (NWO-I/SRON), Niels Bohrweg 4, Leiden, 2333 CA, South Holland, The Netherlands.
E-mail address: zihao.g.yuan@outlook.com (Z. Yuan).

https://doi.org/10.1016/j.jqsrt.2026.109940
Received 10 September 2025; Received in revised form 4 March 2026; Accepted 27 March 2026
Available online 10 April 2026

to three dimensional (3D) radiative transfer effects as well as the above-cloud aerosol and cirrus which causes issues such as CER overestimation [11,14–18]. Nevertheless, the vast majority of satellite-based estimates of the radiative forcing due to aerosol–cloud interactions (RFaci) [19–22] are based on bi-spectral CER retrievals from MODIS. To avoid retrieval biases mentioned above, strict data filtering has been applied [4], which may lead to sampling biases.

Retrievals that make use of measurements of polarized radiance at a high angular resolution (<2°) in the cloud-bow region (scattering angle between $135° - 165°$) have the potential to overcome some of the problems with bi-spectral retrievals [18,23]. Such measurements allow for simple retrieval approach where a Mie single scattering calculations are fitted to the observed polarization measurements, and effects from molecular scattering, aerosols, and cirrus are accounted for by fitting correction terms [23]. Because the polarized radiance is not much affected by higher-order scattering, the retrievals are also not much affected by 3D radiative transfer effects. Hyperangular polarimetric retrievals as described above have been successfully applied to measurements of the airborne Research Scanning Polarimeter (RSP) [11, 24,25]. Similar retrievals have also been performed on measurements of POLDER [26–28] but with limited number of angles (∼10 per native pixel resolution). To achieve high angular resolution, POLDER retrievals use aggregated measurements from level 3 data with regions of approximately 100 km [27]. In addition to the CER, polarimetric measurements also have the capability to provide information on the cloud droplet effective variance (CEV), an important parameter to quantify the so-called dispersion effect of aerosol–cloud interactions [8]. The Hyper-Angular Rainbow Polarimeter-2 (HARP-2) on the Phytoplankton, Aerosol, Cloud & ocean Ecosystems (PACE) [29], launched February 2024, measures polarized radiance at 60 viewing angles at 670 nm, which allows application of the classical cloud-bow retrieval approach to satellite measurements. Given the spectral dependence of the cloud-bow features in polarized radiance [27], hyperspectral measurements of polarized radiance, at a reduced number of viewing angles, may also be expected to have capability for CER and CEV retrieval. Such measurements are provided by the SPEXone instrument [30,31], also on the PACE satellite. SPEXone provides measurements of both intensity and degree of linear polarization (DoLP) for 50 spectral bands at the five viewing angles. Given the more complex contributions of surface reflection, molecular scattering, aerosols and cirrus compared to single-wavelength hyper-angular measurements, a Neural Network (NN) retrieval approach is a suitable candidate for this type of retrievals. NN retrievals have been already successfully applied to multi-angular polarimetric (MAP) measurements for aerosol retrieval [32–35], cloud retrievals [28], and above-cloud aerosol retrievals [36].

This work aims at developing an NN-based CER and CEV retrieval approach from SPEXone measurements and analyzing its sensitivity to different factors including measurement noise, cloud fraction (CF), cloud optical thickness (COT), above-cloud aerosol and cirrus, and 3D radiative transfer effects. The paper is organized as follows: Section 2 shows the polarized radiance's sensitivity to CER and CEV and describe the retrieval methodology. Section 3 analyzes the sensitivity of the retrieval to CF, COT, above-cloud aerosol, above-cloud cirrus and 3D effect. Section 4 summarizes and concludes this study.

2. Polarization and cloud droplet size

To establish the theoretical sensitivity of polarized radiance to cloud microphysical properties, the spectral and angular signatures of single-scattering by cloud droplets are investigated. Fig. 1 shows sun-normalized polarized radiance (normalized relative to incoming solar flux, simply referred as polarized radiance hereafter) of a liquid cloud with different CER and CEV as a function of wavelength and scattering angles in the primary and supernumerary cloud bow region. The CER and CEV are varied while COT and cloud top height (CTH) are fixed (COT = 15, CTH = 1500 m). The radiative contribution from the surface is not considered in the simulation. From Fig. 1 it is clear that both the angular- and spectral dependence of polarized radiance depend on CER and CEV. Conventionally, in hyper-angular polarimetric retrievals, sensitivity of polarized radiance to cloud droplet size is investigated as a function of scattering angle for fixed wavelengths (like Fig. 2 in [23]). In this paper, on the contrary, the sensitivity is investigated as a function of wavelengths for fixed scattering angles, as is depicted in Fig. 2. It can be seen from Fig. 1 that polarized radiance primarily depends on CER and wavelength. The spectral dependence varies as a function of scattering angle, especially at supernumerary bow (150°–160°, where there is a clear CER dependent spectral signal). The sensitivity of the spectrally dependent polarized radiance to CER and CEV (Fig. 2) suggests that the CER can be retrieved from hyperspectral polarimetric measurements if at least one scattering angle is present in the range $140° - 160°$, and CEV can be retrieved if at least one scattering angle is present in the range $150° - 160°$. However, the actual capability to retrieve CER and CEV from multi-angle measurements could be degraded by measurement noise, presence of aerosols and cirrus, and 3D radiative effects. This will be investigated in the remainder of this paper.

3. Methodology

3.1. NN model

In this study, the NN takes polarized radiance and viewing geometries (solar zenith angle, SZA, viewing zenith angle, VZA and scattering angle) as input, with CER and CEV as output. The "neural network ensemble" approach [37] is chosen to increase numerical efficiency and reduce training memory usage. In our settings, the whole training set is equally and randomly divided into several parts, and each part is divided into a training set (90% of the samples) and holdout set (10% of the samples). On each part of the training set, an individual NN is trained. The final output is computed as the average of the output from all the ensembles. Eight ensembles are used for the NN, and each ensemble contains 2 million samples.

As a form of regularization, the noise needs to be applied on the training set [38]. Here it should be noted that the polarized radiance is not directly measured by SPEXone but, instead, calculated as a product of intensity and degree of linear polarization (DoLP), so the noised polarized radiance should be computed as

$$R_{p,noised} = (R_I + \epsilon_I \cdot R_I) \times (\mathrm{DoLP} + \epsilon_{\mathrm{DoLP}}), \tag{1}$$

where ϵ_I and ϵ_{DoLP} are modeled as Gaussian noise. The 1-sigma uncertainty of ϵ_I is 1%–3% and that of ϵ_{DoLP} is 0.002–0.005.

The NNs are implemented using PyTorch (version 2.4.0+cpu, https://pytorch.org/, last access: 09 October 2024) and designed as multi-layer perceptrons (MLPs). The training of the NNs utilizes the back-propagation (BP) algorithm [39] and batch training with a batch size of 12 000. The RAdam optimizer [40], a modification of the Adam optimizer [41] on learning-rate robustness, is employed to minimize the RMSE (root mean square error) loss function. The neural network architecture consists of three hidden layers with 128 neurons in each layer for NN over ocean and 256 neurons for NN over land.

3.2. Description of training set

The training set consists of 16 million samples with a uniformly distributed cloud fraction between 0.2 and 1.0. The training polarized radiance of a partly cloudy pixel is simulated with the independent pixel approximation (IPA) as described in [42]:

$$\begin{cases} Q_{\mathrm{ipa}} = \mathrm{CF} \cdot Q_{\mathrm{cloudy}} + (1 - \mathrm{CF})\ Q_{\mathrm{clear}} \\ U_{\mathrm{ipa}} = \mathrm{CF} \cdot U_{\mathrm{cloudy}} + (1 - \mathrm{CF})\ U_{\mathrm{clear}} \\ R_{p,ipa} = \sqrt{Q_{\mathrm{ipa}}^2 + U_{\mathrm{ipa}}^2} \end{cases}, \tag{2}$$

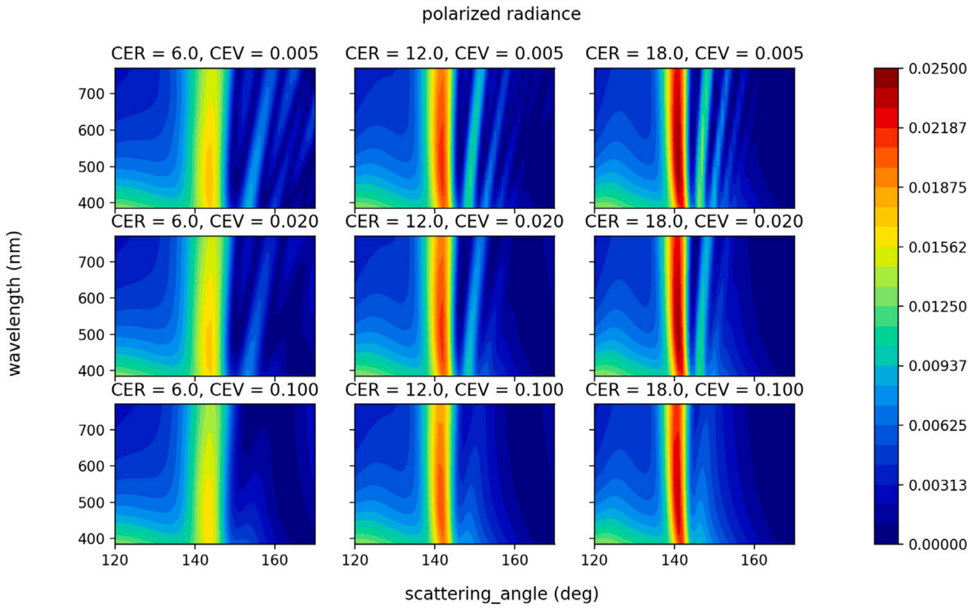

Fig. 1. Sun-normalized polarized radiance of liquid cloud with different CER (μm) and CEV as a function of wavelength (x-axis) and scattering angles (y-axis). From a perspective of hyperspectral retrieval, polarized radiance are sensitive to CER variations and from scattering angle 150° on, polarized radiance is also sensitive to CEV. The polarized radiance is simulated by RemoTAP forward model with plane-parallel homogeneous atmosphere assumption.

The training set consists of 16 million samples with a uniformly distributed cloud fraction between 0.2 and 1.0. In order to consider the radiative contribution from aerosol, cirrus and surface reflection, the aerosol, cirrus and surface properties are varied in the training set. Two separate NNs are trained respectively for cases over ocean and over land. In the training set for the NN over ocean, cirrus optical thickness (CiOT) is uniformly distributed from 0 to 1 for 1/3 of the samples, and for the NN over land 3/4 of the samples are with CiOT uniformly distributed between 0 and 1. The rest of training set samples are cirrus-free. More cirrus samples are included for the training over land because of the larger sensitivity to cirrus of these retrievals (see below).

The synthetic measurements for the NN training are generated by the RemoTAP forward model [43–45], a linearized radiative transfer model in the RemoTAP retrieval algorithm [31,46–49]. The liquid cloud optical properties are computed using a Mie code [50] assuming particles with a Gamma size distribution, and the refractive index of water is from [51]. The ice cloud modeling uses hexagonal crystals with varying aspect radios and surface distortions for variable-complex-shaped ice crystals [52]. The aerosol size distribution follows three log-normal modes, as in [49]. Each mode is described by effective radius, effective variance, aerosol optical thickness (AOT) at 550 nm, complex refractive index (wavelength dependent), aerosol layer height and fraction of spherical particles. Aerosol optical properties are computed using the Mie/T-Matrix tables of [53]. The land surface simulation is based on the bidirectional reflectance distribution function (BRDF), parameterized using the Ross-Li model [54,55], and the bidirectional polarization distribution function (BPDF), parameterized as in [56]. For the ocean surface, the reflection properties are parameterized based on chlorophyll-a concentration as described in [57] for the ocean body contribution and a Fresnel contribution from the ocean surface following the wind-speed dependent description of surface slopes of [58].

The surface (land and ocean) parameters for the NN training are from randomly picked pixels of PARASOL-RemoTAP global retrieval [59] for the year 2008. Because of the sparse spectral coverage of the PARASOL-RemoTAP surface albedo, the surface albedo for the 50 SPEXone spectral bands are calculated by combining GOME-2 climatology [60] with PARASOL-RemoTAP retrievals as:

$$\alpha_\lambda = \alpha_{\lambda,g} \cdot \frac{\alpha_{670,p}}{\alpha_{670,g}}, \tag{3}$$

where α_λ is the surface albedo at wavelength λ (nm) and the subscript g and p stand for GOME-2 and PARASOL-RemoTAP respectively. The cloud properties are generated randomly. The aerosol properties are randomly picked from PARASOL-RemoTAP global retrievals [59] in 2008. The geometry (SZA, VZA and scattering angle) are taken from simulated SPEXone orbits. Only the measurements with five angles are considered for the NN training. A detailed statistical distribution of the training set can be found in Table A.1.

4. Sensitivity analysis

4.1. Description of synthetic validation data sets

Independent validation sets are created to check the performance of the NN retrieval. Besides the variation of liquid cloud properties, the validation set also considers variation of surface, aerosol properties, viewing geometries and cloud fraction (0.2–1.0). These validation sets aim to assess the influence on NN's performance by CF and COT, above-cloud aerosols, cirrus and 3D effects.

4.1.1. Basic validation set

This validation set (50,000 samples) uses a similar settings as the training set (as in Section 3.2) while it does not consider cirrus (although it is included in the training set). A detailed description of the validation sets can be found in Table B.2.

4.1.2. Validation set for above-cloud aerosol sensitivity

To investigate the sensitivity of cloud retrievals to above-cloud aerosol optical thickness (ACAOT), synthetic SPEXone measurements are simulated for a range of ACAOT values across two distinct aerosol type regimes: fine-mode-dominated (where 90% of the total ACAOT is contributed by fine mode aerosols) and dust-mode-dominated (where 90% is contributed by dust mode aerosols). For each combination of ACAOT value, aerosol type, and cloud fraction (CF = 1.0 for overcast or CF = 0.5 for partly cloudy), 1000 synthetic measurements are generated. Within each data set, the specified ACAOT, aerosol type, and cloud fraction are held constant, while cloud microphysical properties (CER, CEV, COT, CTH), aerosol microphysical properties (size, refractive index), surface reflectance, and viewing geometries are varied according to the baseline distributions outlined in the basic validation set (Section 4.1.1).

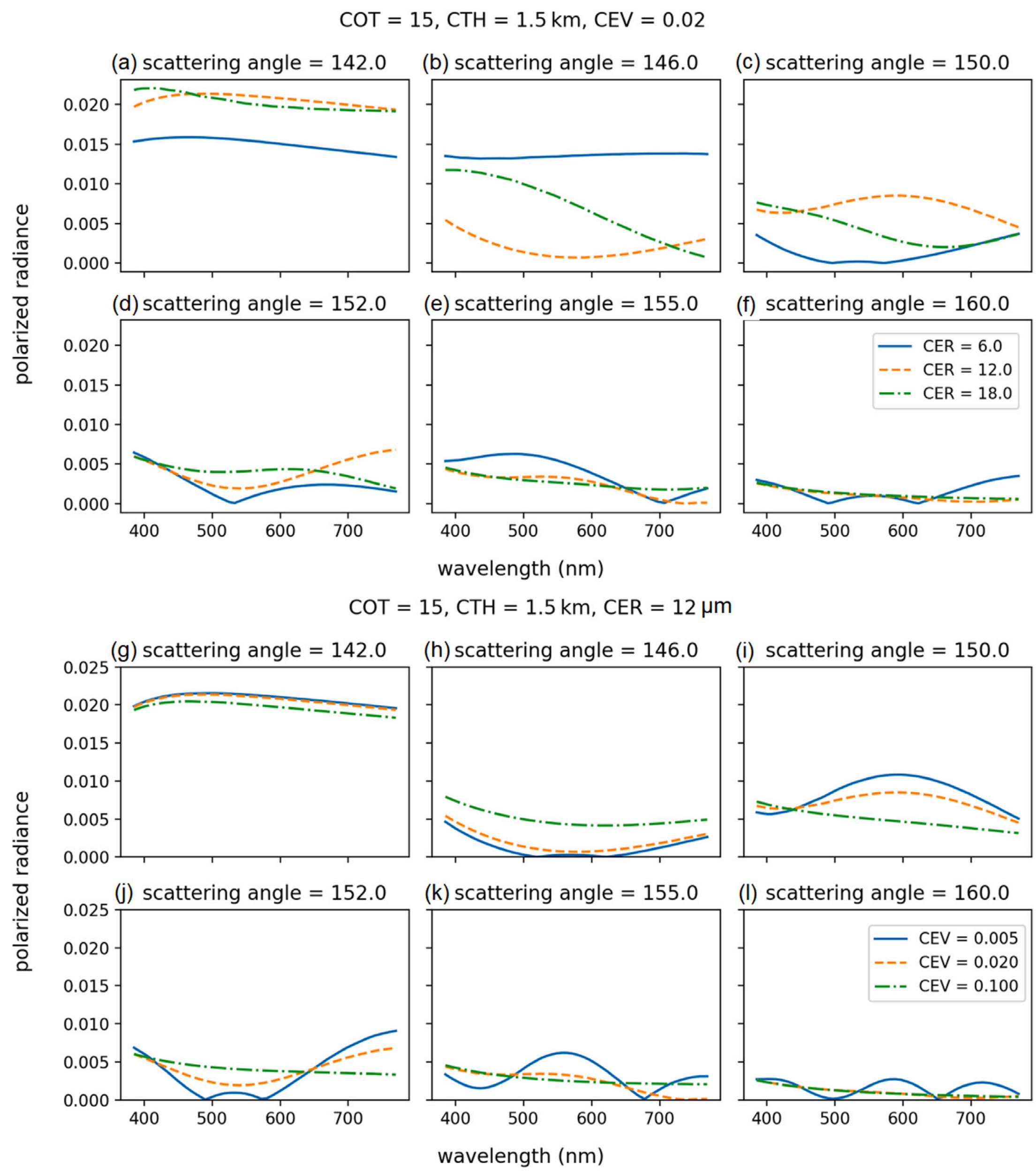

Fig. 2. Polarized radiance of liquid cloud with different CER (μm) and CEV as a function of wavelength under six scattering angles. Under all the six scattering angles, polarized radiance are sensitive to CER variations and from scattering angle 150° on, polarized radiance is also sensitive to CEV.

4.1.3. Validation set for cirrus sensitivity

For the sensitivity analysis to cirrus clouds, multiple synthetic data sets are generated, each corresponding to a unique, fixed value of cirrus optical thickness (CiOT) and CF. Within each dataset, the designated CiOT and CF (either fully overcast, CF = 1.0, or partly cloudy, CF = 0.5) are held constant, while other cloud properties (CER, CEV, COT, CTH), surface reflectance, and viewing geometries are varied. All datasets follow the same foundational configuration as the primary validation set described in Section 4.1.1.

4.1.4. Simulated 1D and 3D measurement of a cloud field

To study the influence of 3D radiative transfer effects on the retrieval, a synthetic cloud field with a size of 40 km × 40 km is generated. In the cloud field, each pixel for the 3D forward model is 1 km × 1 km, and all the clouds are with CER = 10 μm, CEV = 0.02, COT = 10, cloud bottom height, CBH = 1 km, and the CTH varies between 1.2 to 1.8 km. Such a simplified cloud field is chosen over e.g., a large eddy simulation (LES) in order to isolate the effect of 3D radiative transfer and not to mix it with other effects, such as the effect of subpixel variation of the cloud properties. The generated cloud field is used as input to the MYSTIC 3D radiative transfer model [61] to generate top-of-atmosphere radiances and polarized radiances at 27 wavelengths (which are further interpolated to the full wavelength grid) and five viewing angles. To simulate SPEXone pixels, five by five 1 × 1 km^2 pixels are averaged from the calculation at 1 km sampling. The 1D measurement is simulated by RemoTAP forward model on a resolution of 5 km × 5 km, with IPA used for partly cloudy pixels. To avoid inconsistencies in the surface BRDF and BPDF between MYSTIC and the RemoTAP forward model, the errors are translated by applying the difference between 3D and 1D MYSTIC calculations to the RemoTAP forward calculation for each scene.

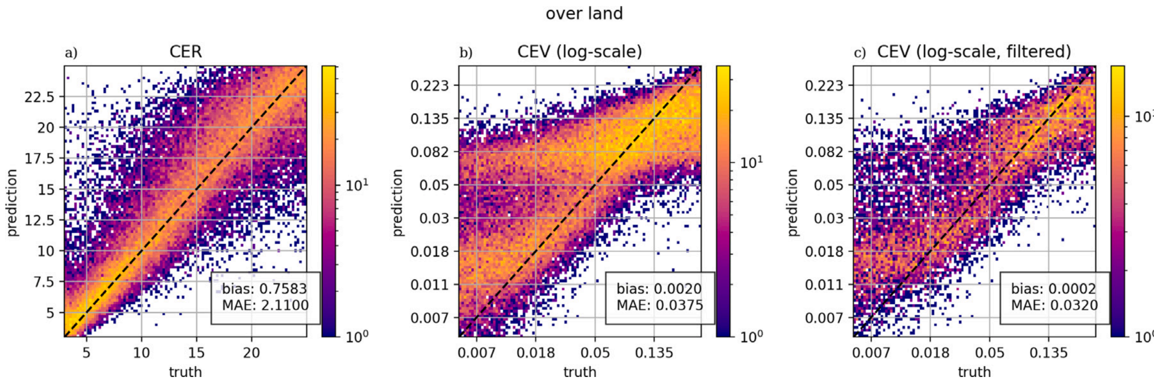

Fig. 3. Density scatter plot of CER (panel a) and CEV (panel b) retrieval compared with truth on the synthetic validation set over land. Panel c is the CEV retrieval on pixels where CER < 10 μm. The color stands for the number of points in a same grid. The axes of the CEV plots are in log scale.

4.2. Synthetic results

As an overall assessment of NN's performance, the NN is applied on the basic evaluation set (as is described in Section 4.1.1). Fig. 3 depicts the CER and CEV retrieval on the validation set over land compared with their truth. The CER retrieval by the NN algorithm yields a Mean Absolute Error (MAE) of 2.11 μm. The CEV retrieval gives an MAE of 0.0375. The NN performs similar over ocean as over land, with MAE of 2.03 on CER and 0.0342 on CEV (not shown in the figure). There are two branches in 2-D density distribution (panel b, Fig. 3), one following close to one-to-one line, and another presenting the prediction between ∼0.05 and 0.15 whereas the truth varies between 0.005 and 0.3. The interpretation is that first branch corresponds to the pixels with good skill in CEV retrieval, and the other branch to the pixels with low skill of retrieval. The later branch of pixels is well screened out when retrievals with CER > 10 μm are excluded (panel c, Fig. 3), as a larger CER will damp the spectral dependent signal in supernumerary bows which is sensitive to CEV retrieval (see Figure S2 in SI).

The retrieval capability as a function of CF and COT is also investigated, as they influence largely to the polarized radiance of clouds in a given pixel. Eight bins are defined for CF and COT respectively, and the MAE of CER and CEV retrievals from validation samples (the basic validation set, as is described in Section 4.1.1) that fall into each of 64 bins are presented by color shading in Fig. 4. The error on CER and CEV, over both ocean and land, decreases as the CF increases, because the contribution of the cloud to the measured polarized radiance increases. However, the MAE does not decrease monotonically with COT, and it reaches a minimum CER error for COT in the range between ∼3 and 12 and a minimum CEV error for COT between ∼3 and 5. The initial decrease in MAE with increasing COT from 1 to 5 can be explained by the increasing contribution of the cloud to the measured polarized radiance. However, the polarized radiance starts to saturate at around COT = 5, whereas the total radiance continues to increase even for COT values greater than 20 [62]. Consequently, the signal-to-noise ratio (SNR) of the polarized radiance decreases as the total radiance increases with COT, since a higher total radiance contributes a greater absolute noise level (see Eq. (1)). Overall, it can be concluded that the CER can be retrieved with an MAE < 2 μm for CF > 0.6 and COT between 2 and 12 over both ocean and land. The CEV can be retrieved over ocean with an MAE < 0.035 for CF > 0.6 and COT between 2 and 8, and over land for CF > 0.7 and COT between 2 and 5.

4.3. Sensitivity to above-cloud aerosols

In this section, the NN is applied on the validation set described in Section 4.1.2 to investigate the sensitivity to above-cloud aerosols. The retrieval is applied on the 1000 synthetic measurements for each ACAOT value, and the MAE as well as the bias of CER and CEV over land are shown in Fig. 5. As the ACAOT increases from 0.0 to 1.0, the MAE of the CER for the fine-mode-dominated case (panel a) increases from below 2 μm at ACAOT = 0 to MAE = ∼5 μm for ACAOT = 1, and shows a similar pattern for the fully and partly cloudy scene. It can be seen that a substantial part of the MAE comes from a positive bias (panel b) in the CER, which increases to ∼2 at ACAOT = 1. For the CEV, the MAE (panel c) increases from 0.0317 at ACAOT = 0 to MAE = 0.0570 at ACAOT = 1 for the fully cloudy case and from 0.0363 to 0.0616 for the partly cloudy case. For the dust-mode-dominated aerosols, the MAE for CER (panel e) is lower than that for the fine-mode-dominated aerosols at lower ACAOT (<0.4), but for the partly cloudy case, the MAE reaches the same value (∼5 μm) at ACAOT = 1. For the fully cloudy case, the CER MAE for the dust-dominated aerosols is lower than for the fine-mode-dominated aerosols for all ACAOT values. The CEV MAE look very similar for the fine-mode-dominated (panel c) and dust-dominated cases (panel g). The performance over ocean are similar to that over land.

The spectral feature difference in polarized radiance between the fine mode and dust mode may cause the difference in performance for CER (lower error under dust-than fine-mode-dominated cases). The polarized radiance as a function of wavelength and scattering angle for both fine-mode-dominated aerosol above cloud and dust-mode-dominated aerosol are shown in Fig. 6, for different ACAOT values. All other aerosol and cloud properties are fixed in this figure. Both fine mode aerosol and dust mode aerosol have an obvious extinction effect on the cloud bow, but the fine mode aerosol's effect is stronger. A heavy fine-mode-dominated aerosol load (e.g., ACAOT = 0.5) interferes with the spectral feature of the underlying cloud, and hence negatively affects the retrieval capability.

4.4. Sensitivity to above-cloud cirrus

In this section, the NN retrieval algorithm is applied to the validation data set described in Section 4.1.3 to assess its performance under varying cirrus contamination. Fig. 7 depicts the MAE and bias of CER and CEV as a function of CiOT for partly cloudy (CF = 0.5) and fully cloudy scenes over ocean and over land. For partly cloudy scene over both land and over ocean, the MAE on CER and CEV increases strongly with CiOT. However, over fully cloudy scenes, the error is less sensitive to CiOT, especially over ocean, showing capability to retrieve CER with an MAE < 2.5 μm for CiOT up to 0.3. Over land, the MAE on CER is similar to that over ocean for cirrus-free scenes, but the MAE steeply increases to 2.616 μm at CiOT = 0.02. The MAE stays almost constant at ∼2.7 μm till CiOT = 0.2, but then increases to >3 μm at CiOT = 0.3. The MAE of CEV follows a similar pattern as a function of CiOT as the CER over both ocean and land. Overall, it can be concluded that our approach has capability to retrieve liquid cloud CER and CEV for cirrus contaminated pixels when the pixel is fully covered by the liquid cloud

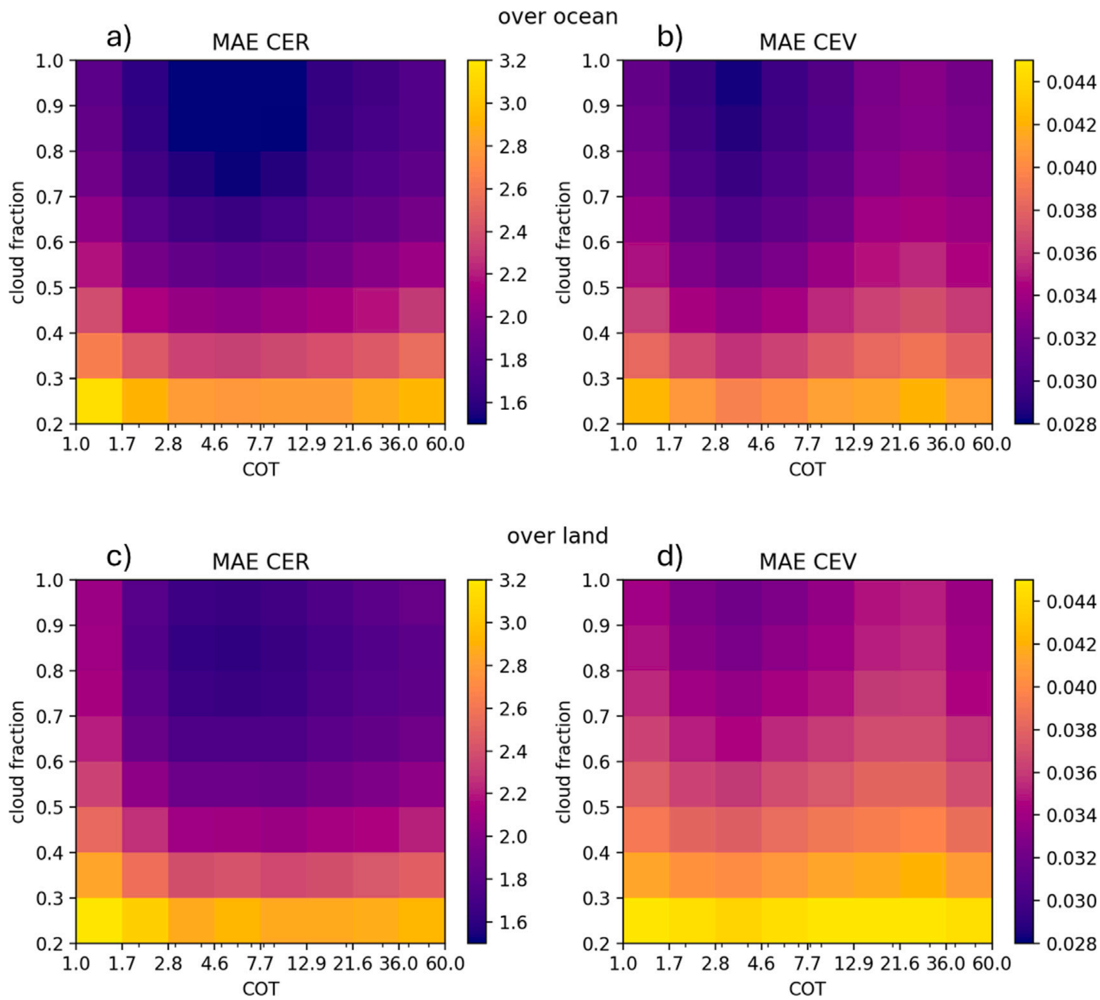

Fig. 4. The MAE of CER (a, c) and CEV (b, d) as a function of liquid cloud fraction and liquid cloud optical thickness over ocean (a, b) and over land (c, d).

(with CER MAE < 3 μm and CEV MAE < 0.040 when CiOT < 0.15). Over ocean, for very thin cirrus (CiOT < 0.1), retrievals can still be performed for partly cloudy cases (with CER MAE < 3.5 μm and CEV MAE < 0.045), but retrievals over land have large retrieval errors for partly cloudy scenes contaminated by cirrus. Overall, both over ocean and over land, cirrus contamination leads to an overestimation in CER retrieval.

4.5. Influence of 3D effect

As is described in Section 4.1.4, synthetic measurements over a cloud field are calculated respectively by 1D and 3D radiative transfer model. An RGB image of the calculated synthetic measurements is shown in Fig. 8, where a significant 3D effect can be well observed from the five different viewing angles. In Fig. 9, one SPEXone pixel from the cloud field is selected and the radiance and polarized radiance from 1D (computed by the independent pixel approximation) and 3D calculation is shown for five viewing angles. The simulated radiances from 3D and 1D radiative transfer calculations differ greatly (with a relative difference of 12.73%), but the 3D and 1D simulations for polarized radiance are much more similar (with a relative difference of 2.80%). This confirms that polarized radiance has a much smaller sensitivity to 3D radiative transfer effect than total radiance.

This behavior can be explained by the fact that polarized radiance originates from low order scattering (dominated by single scattering) because light gets depolarized for higher order scattering. In contrast, total reflectance is the result of all scattering orders, with 3D radiative effects in total reflectances being dominated by higher order multiple scattering. Multiple scattering events cause radiation to be redistributed with increasingly disoriented scattering planes, creating solar zenith and azimuth angle-dependent illumination and shadowing effects. Single scattering-dominated signals are therefore less sensitive to 3D radiative effects because they lack these geometry-dependent illumination and shadowing biases, instead sampling primarily the phase function (P11 or P12 elements) as a function of scattering angle alone. This principle also provides a physical basis for the behavior observed in other spectral domains. For example, the reduced sensitivity to 3D effects in shortwave infrared (SWIR) bands, which have stronger liquid water absorption, occurs because absorption preferentially attenuates photons undergoing longer, multiple-scattering paths. This leaves a reflectance signal more characteristic of single scattering. This nuance is particularly relevant for classical bi-spectral cloud retrievals (e.g., using VIS and SWIR channels), as the differing 3D sensitivity between the bands can introduce biases when the retrieval assumes a 1D radiative transfer model. It has to be noted that polarized radiance is still affected by 3D effects, but this effect mainly happens in the cloudbow and the glory but generally are smaller at larger spatial scale (>1 km, [63]).

To verify whether this insensitivity translates to the retrieved microphysical properties, the retrievals are performed on the modified (3D) RemoTAP synthetic measurements, and the results are compared with the retrievals on the corresponding RemoTAP 1D synthetic measurements. The error (truth–prediction) of the CER and CEV retrievals are plotted in Fig. 10 as a function of CF. No significant difference between retrievals on 1D and 3D measurement is observed, as both the CER and the CEV retrievals give similar MAE and bias for 1D and 3D synthetic measurements.

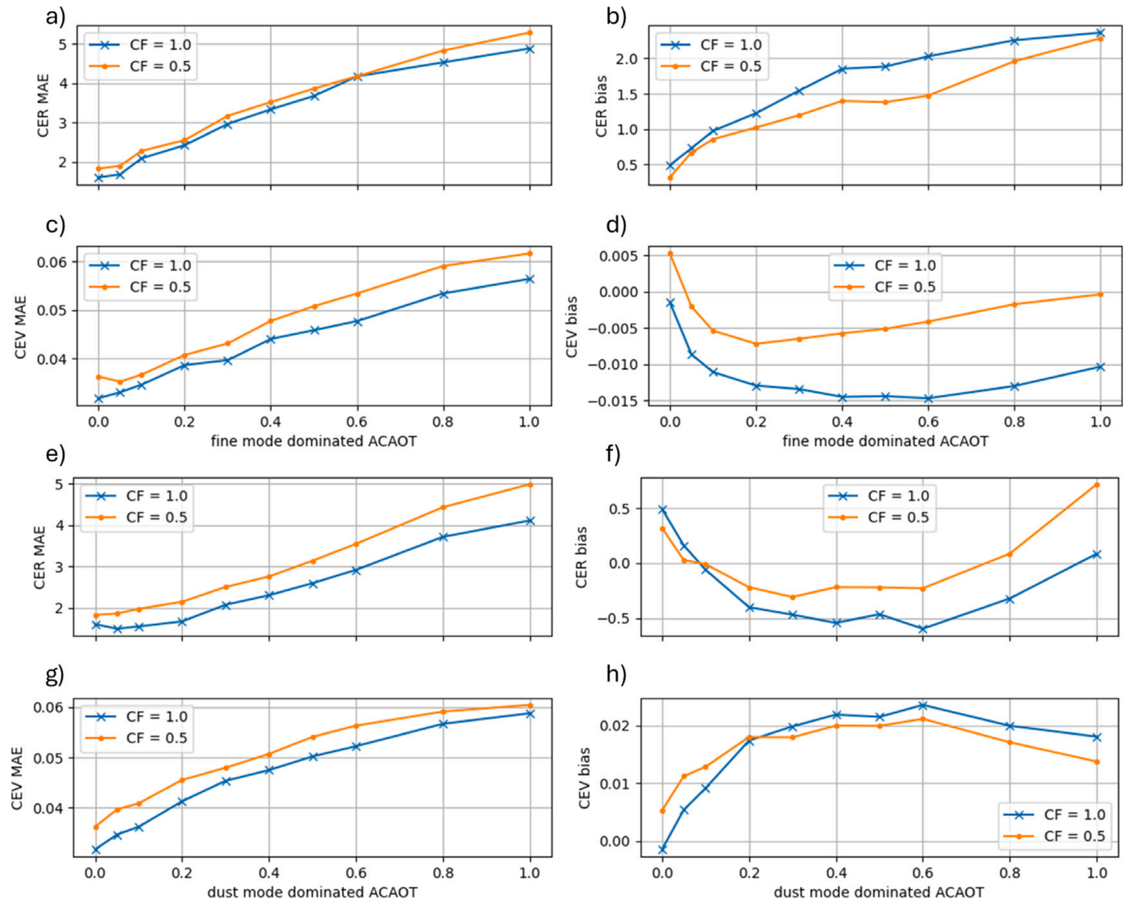

Fig. 5. The MAE of CER (a, e) and CEV (c, g), bias of CER (b, f) and CEV (d, h), as a function of above cloud aerosol optical thickness over land for both fine-mode-dominated (a, b, c, d) and dust-mode-dominated aerosols (e, f, g, h).

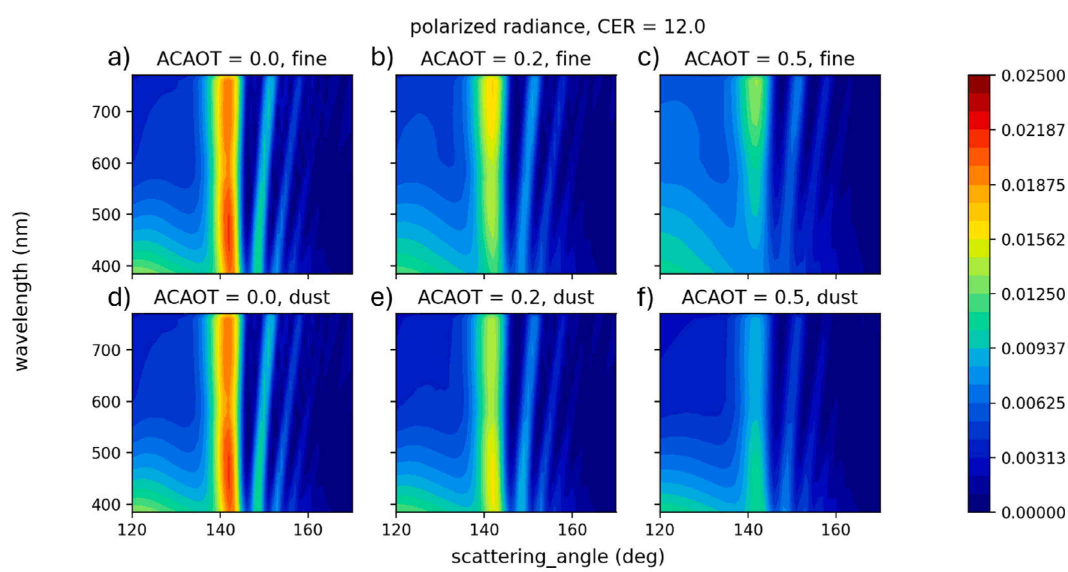

Fig. 6. Polarized radiance of fine-mode-dominated (a, b, c) and dust-mode-dominated (d, e, f) ACA scenes as a function of scattering angle and wavelengths for different CER and ACAOT. Other cloud and aerosol properties are fixed: CEV = 0.005, COT = 15, CTH = 1500 m, aerosol layer height, ALH = 6000 m, fine mode aerosol with an effective radius of 0.1 μm and effective variance of 0.2, and dust mode aerosol with an effective radius of 1.5 μm and effective variance of 0.2. The imaginary part of dust is 0.05, and of fine mode component black carbon and organic carbon is 0.01 and 0.1 respectively.

5. Conclusion and discussion

In this paper, an NN approach of CER and CEV retrieval from SPEXone hyperspectral multi-angle polarimetric measurements is proposed, and the capability of the approach is analyzed. The training of the NN considers the variation of cloud fraction, aerosol and cirrus properties, as well as surface properties, without explicitly retrieving them. Separate NNs are trained for retrievals over land and ocean respectively.

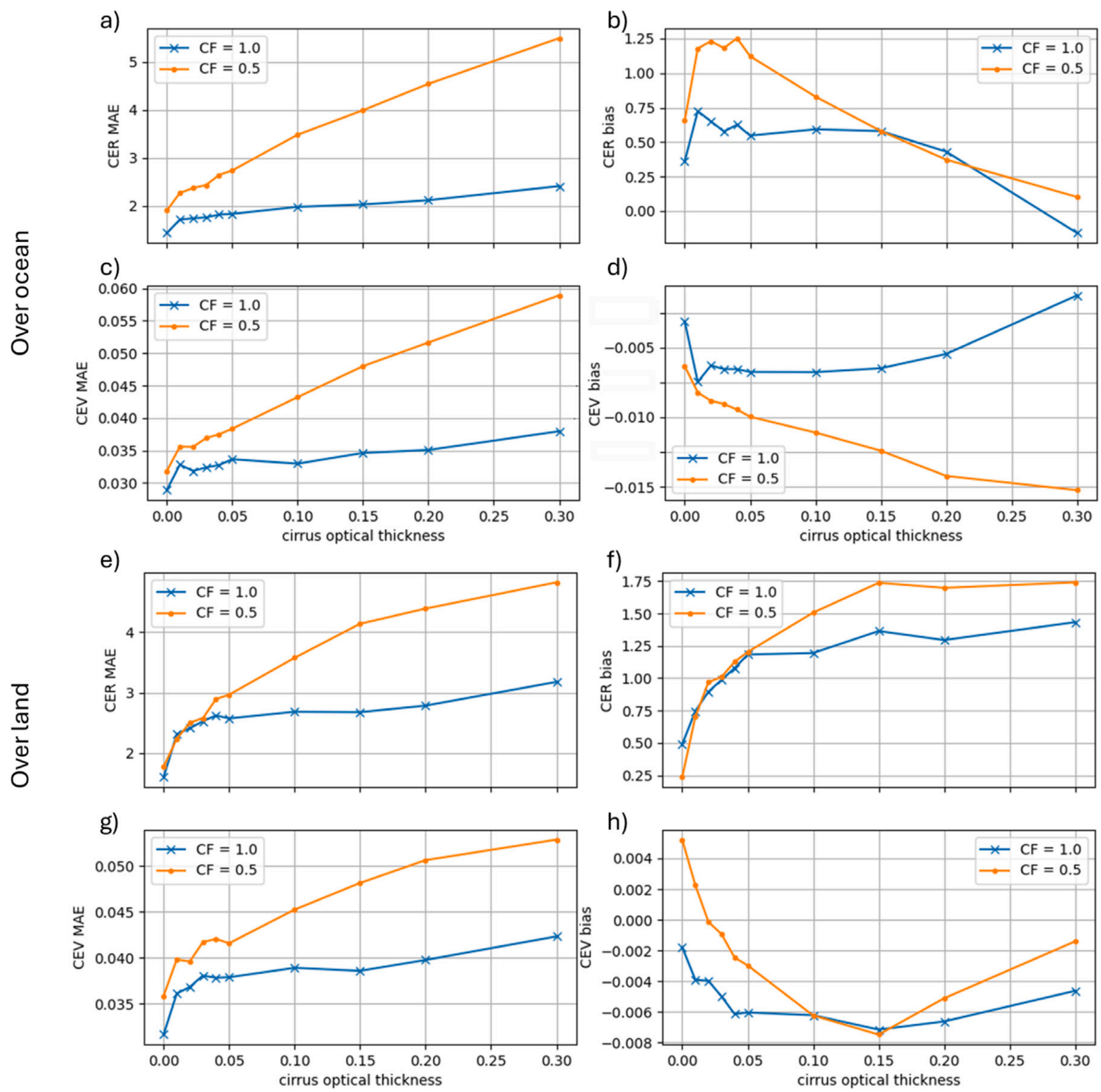

Fig. 7. The MAE of CER (a, e) and CEV (c, g), bias of CER (b, f) and CEV (d, h), as a function of above cloud cirrus optical thickness over ocean (a, b, c, d) and over land (e, f, g, h).

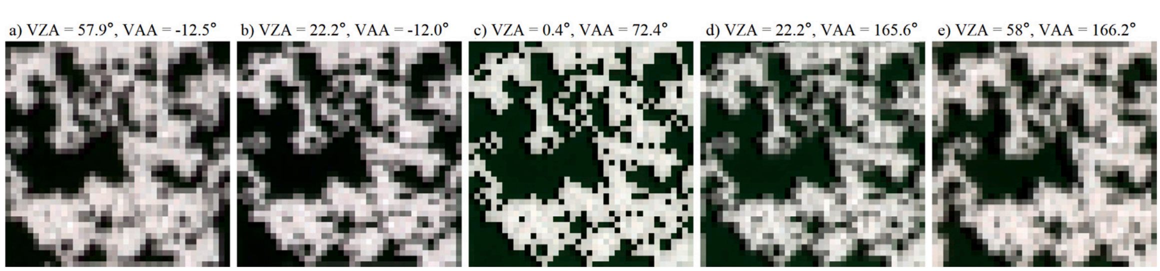

Fig. 8. Simulated RGB images of cloud field viewed by the five viewing ports. SZA = 31° and SAA = −162.4°. The clouds are with CER = 10, CEV = 0.02, COT = 10, CBH = 1 km, and the CTH varies between 1.2 to 1.8 km. The 3D effect causes the difference among these images.

The NN takes hyperspectral polarized radiance at five viewing angles together with the solar-viewing geometry as input. The CER and CEV for liquid clouds are yielded as output by the NN. Validation with an independent data set demonstrates the capability to retrieve CER with an MAE of 2.11 μm and CEV with an MAE of 0.0375 over land. A similar performance can be achieved over ocean.

It is found that retrieval errors are strongly influenced by CF and COT. Errors decrease with increasing CF, but not monotonically with increasing COT. The lowest errors appear for CER when COT is between ∼3 and 12, while for CEV at COT between ∼3 and 5. At higher COT, the error increases due to the saturation of polarized radiance and the corresponding lower SNR. Overall, it can be concluded that the CER

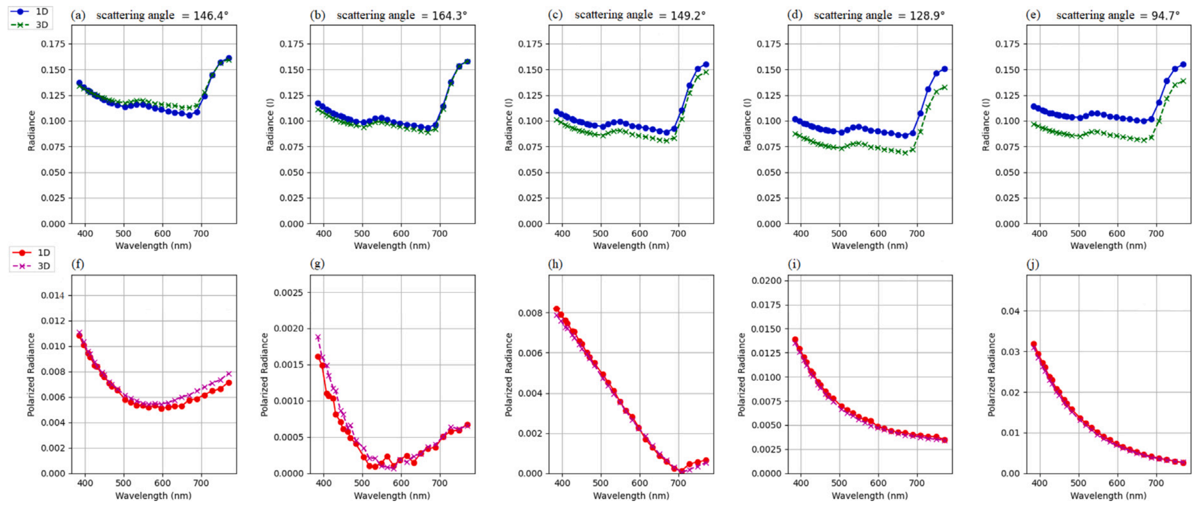

Fig. 9. Radiance and polarized radiance from 1D and 3D radiative transfer simulation on one 5 km × 5 km pixel in the cloud field, where cloud fraction is 0.72. The radiance differs largely on all the viewing angles and wavelengths while the polarized radiance shows a small discrepancy. At some angles the difference between 1D and 3D simulations for total radiance is much larger than others (panel d,e), but such behavior is not observed for the polarized reflectance.

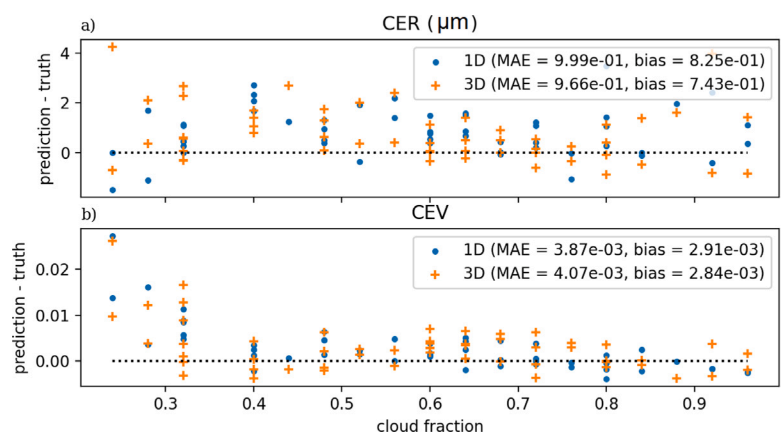

Fig. 10. Error (prediction–truth) of retrieval from RemoTAP-1D synthetic measurement (blue dots) and MYSTIC-3D synthetic measurement (orange crosses) on the cloud field.

can be retrieved with an MAE < 2 μm for CF > 0.6 and COT between 2 and 12 over both ocean and land. The CEV can be retrieved over ocean with an MAE < 0.035 for CF > 0.6 and COT between 2 and 8, and over land for CF > 0.7 and COT between 2 and 5.

The sensitivity study on above-cloud aerosol reveals that increasing aerosol load above clouds degrades retrieval accuracy. Over land, for partly cloudy scenes, the MAE of CER increases from ~2 to 5 μm and the MAE of CEV from ~0.03 to 0.06 as the ACAOT increases from 0.0 to 1.0. Fully cloudy scenes show a similar trend. At low ACAOT, dust-mode aerosols lead to lower errors than fine-mode aerosols, especially for CER, but this difference diminishes at ACAOT > 0.8. The stronger extinction effect of fine-mode aerosols on the cloud bow disrupts the spectral signal used in retrieval, leading to significant error increases. Overall, the CER can be retrieved with an MAE < 2 μm if the ACAOT < 0.1 for fine-mode-dominated aerosols and ACAOT < 0.2 for dust-mode-dominated aerosols.

The sensitivity study on above-cloud cirrus indicates that the retrieval method is more vulnerable to cirrus contamination under partly cloudy conditions, than fully cloudy conditions. Over both land and ocean, CER and CEV errors increase sharply with CiOT in partly cloudy scenes. In contrast, fully cloudy scenes show reduced sensitivity to cirrus, particularly over ocean, where the MAE of CER increases modestly from 1.427 μm (CiOT = 0) to 2.407 μm (CiOT = 0.3). Over land, MAE of CER remains stable at ~2.7 μm for CiOT between 0.01 and 0.2 but exceeds 3 μm at CiOT = 0.3. Even very thin cirrus layers (CiOT = 0.01) cause noticeable error increases over partly cloudy scenes, with a greater impact over land than ocean. The MAE of CEV exhibits a similar trend.

The NN has also been applied on synthetic measurements taking into account 3D radiative transfer effects from the MYSTIC 3D model for a broken cloud scene. The MAE and bias of both CER and CEV does not show a significant difference, between 3D and 1D synthetic measurements created for the same cloud field. This suggests that the retrieval method is robust against 3D effects under the tested conditions.

This study demonstrates the capability of SPEXone hyperspectral measurements at five viewing angles to provide liquid cloud CER and CEV retrievals. The next step will be to apply this approach to real SPEXone observations and evaluate against hyperangular retrievals from the HARP-2 instrument and the bi-spectral retrievals from OCI. Having three different sets of CER retrievals and two sets of CEV retrievals from the same satellite will help to identify the strength and weakness of each product, with the potential to improve individual products. It also allows to perform ACI studies [19–22] with the three different products, giving insight to the impact of cloud retrieval uncertainty on the resulting radiative forcing due to ACI (RFaci).

Table A.1
Details of the statistical distributions of the aerosol and cloud parameters used to generate the training datasets. Distribution of "RemoTAP" means properties are randomly taken from 2008 PARASOL-RemoTAP L2 database.

Parameter	Min	Mmax	Mean	Distribution
Wind speed (m/s)	0.1	87	7.52	RemoTAP
chl-α concentration	0.001	10	1.92	RemoTAP
Li-sparse	0	0.35	0.14	RemoTAP
Ross-thick	0	1.4	0.41	RemoTAP
Maignan bpdf	0.2	10	3.02	RemoTAP
brdf scaling coefficient (443 nm)	0	0.40	0.06	RemoTAP
brdf scaling coefficient (490 nm)	0	0.45	0.10	RemoTAP
brdf scaling coefficient (565 nm)	0	0.50	0.17	RemoTAP
brdf scaling coefficient (670 nm)	0	0.65	0.23	RemoTAP
brdf scaling coefficient (865 nm)	0	0.80	0.33	RemoTAP
brdf scaling coefficient (1020 nm)	0	0.90	0.37	RemoTAP
Effective radius of liquid cloud (μm)	3	30	16.5	Uniform
Effective variance of liquid cloud	0.005	0.3	0.07	Log-uniform
Cloud optical thickness of liquid cloud	1	60	14.4	Log-uniform
Cloud layer height of liquid cloud (km)	0.5	6	2.2	Uniform in pressure space
Effective radius of ice cloud (μm)	10	60	30	Uniform
Cloud optical thickness of ice cloud	0	1	0.5	Uniform
Cloud layer height of ice cloud (km)	8	17	9.5	Uniform
Aspect ratio of ice cloud crystals	0.179	5.592	1.57	Log-uniform
Distortion of ice cloud crystals	0.1	0.7	0.4	Uniform
Aerosol effective radius of fine mode	0.02	0.57	0.14	RemoTAP
Aerosol effective variance of fine mode	0.01	0.8	0.20	RemoTAP
Aerosol optical thickness of fine mode	0	1.58	0.11	RemoTAP
Aerosol effective radius of dust mode	0.7	6.12	1.89	RemoTAP
Aerosol effective variance of dust mode	0.01	0.8	0.58	RemoTAP
Aerosol optical thickness of dust mode	0	2.11	0.15	RemoTAP
Aerosol effective radius of soluble mode	0.7	6.12	3.24	RemoTAP
Aerosol effective variance of soluble mode	0.01	0.8	0.59	RemoTAP
Aerosol optical thickness of soluble mode	0	0.86	0.002	RemoTAP

CRediT authorship contribution statement

Zihao Yuan: Writing – original draft, Software, Methodology. **Bastiaan van Diedenhoven:** Writing – review & editing, Methodology, Investigation. **Guangliang Fu:** Writing – review & editing, Software. **Hai Xiang Lin:** Writing – review & editing, Resources. **Jan Willem Erisman:** Writing – review & editing, Resources. **Otto P. Hasekamp:** Writing – review & editing, Supervision, Resources, Project administration, Methodology, Investigation, Conceptualization.

Financial support

BvD acknowledges support from the Dutch Research Council (NWO), The Netherlands and the Netherlands Space Office (NSO) (grant no. ALWGO.2019.006).

Declaration of competing interest

The authors declare the following financial interests/personal relationships which may be considered as potential competing interests: Zihao Yuan reports financial support was provided by China Scholarship Council. Bastiaan van Diedenhoven reports financial support was provided by Dutch Research Council. If there are other authors, they declare that they have no known competing financial interests or personal relationships that could have appeared to influence the work reported in this paper.

Acknowledgment

ZY acknowledges the support of the China Scholarship Council (No. 202106220072). The authors also thank SURFsara, the Netherlands Supercomputing Centre in Amsterdam, for providing the Spider cluster as the computing facility in the NN training experiments (EINF-14047).

Appendix A. Statistical distributions of the training set

See Table A.1.

Appendix B. Statistical distributions of the validation set

See Table B.2.

Table B.2
Details of the statistical distributions of the aerosol and cloud parameters used to generate the validation datasets. Distribution of "RemoTAP" means properties are randomly taken from 2008 PARASOL-RemoTAP L2 database.

Parameter	Min	Max	Mean	Distribution
Wind speed (m/s)	0.1	87	7.52	RemoTAP
chl-α concentration	0.001	10	1.92	RemoTAP
Li-sparse	0	0.35	0.14	RemoTAP
Ross-thick	0	1.4	0.41	RemoTAP
Maignan bpdf	0.2	10	3.02	RemoTAP
brdf scaling coefficient (443 nm)	0	0.40	0.06	RemoTAP
brdf scaling coefficient (490 nm)	0	0.45	0.10	RemoTAP
brdf scaling coefficient (565 nm)	0	0.50	0.17	RemoTAP

(*continued on next page*)

Table B.2 (*continued*).

Parameter	Min	Max	Mean	Distribution
brdf scaling coefficient (670 nm)	0	0.65	0.23	RemoTAP
brdf scaling coefficient (865 nm)	0	0.80	0.33	RemoTAP
brdf scaling coefficient (1020 nm)	0	0.90	0.37	RemoTAP
Effective radius of liquid cloud (μm)	3	25	14	Uniform
Effective variance of liquid cloud	0.005	0.3	0.07	Log-uniform
Cloud optical thickness of liquid cloud	1	60	14.4	Log-uniform
Cloud layer height of liquid cloud (km)	0.5	6	2.2	Uniform in pressure space
Effective radius of ice cloud (μm)	10	60	30	Uniform
Cloud optical thickness of ice cloud	N/A	N/A	N/A	Experimentally specific
Cloud layer height of ice cloud (km)	8	17	9.5	Uniform
Aspect ratio of ice cloud crystals	0.179	5.592	1.57	Log-uniform
Distortion of ice cloud crystals	0.1	0.7	0.4	Uniform
Aerosol effective radius of fine mode	0.02	0.57	0.14	RemoTAP
Aerosol effective variance of fine mode	0.01	0.8	0.20	RemoTAP
Aerosol optical thickness of fine mode	0	1.58	0.11	RemoTAP
Aerosol effective radius of dust mode	0.7	6.12	1.89	RemoTAP
Aerosol effective variance of dust mode	0.01	0.8	0.58	RemoTAP
Aerosol optical thickness of dust mode	0	2.11	0.15	RemoTAP
Aerosol effective radius of soluble mode	0.7	6.12	3.24	RemoTAP
Aerosol effective variance of soluble mode	0.01	0.8	0.59	RemoTAP
Aerosol optical thickness of soluble mode	0	0.86	0.002	RemoTAP

Appendix C. Supplementary data

Supplementary material related to this article can be found online at https://doi.org/10.1016/j.jqsrt.2026.109940.

Data availability

Data will be made available on request.

References

[1] Arias Paola, Bellouin Nicolas, Coppola Erika, Jones Christopher, Krinner Gerhard, Marotzke Jochem, Naik Vaishali, Plattner Gian-Kasper, Rojas Maisa, Sillmann Jana, Storelvmo Trude, Thorne Peter, Trewin Blair, Achutarao Krishna, Adhikary Bhupesh, Armour Kyle, Bala Govindasamy, Barimalala Rondrotiana, Berger Sophie, Zickfeld Kirsten. Climate change 2021: The physical science basis. Contribution of working group I to the sixth assessment report of the intergovernmental panel on climate change; technical summary. 2021.

[2] Myers Timothy A, Norris Joel R. Reducing the uncertainty in subtropical cloud feedback. Geophys Res Lett 2016;43(5):2144–8. http://dx.doi.org/10.1002/2015GL067416, URL https://agupubs.onlinelibrary.wiley.com/doi/abs/10.1002/2015GL067416.

[3] Tan Ivy, Zhou Chen, Lamy Aubert, Stauffer Catherine L. Moderate climate sensitivity due to opposing mixed-phase cloud feedbacks. Npj Clim Atmospheric Sci 2025;8:86. http://dx.doi.org/10.1038/s41612-025-00948-7.

[4] Gryspeerdt Edward, Povey Adam C, Grainger Roy G, Hasekamp Otto, Hsu Nai-Yung C, Mulcahy Jane P, Sayer Andrew M, Sorooshian Armin. Uncertainty in aerosol–cloud radiative forcing is driven by clean conditions. Atmospheric Chem Phys 2023;23:4115–22. http://dx.doi.org/10.5194/acp-23-4115-2023.

[5] Rosenfeld D, Kokhanovsky A, Goren T, Gryspeerdt E, Hasekamp O, Jia H, Lopatin A, Quaas J, Pan Z, Sourdeval O. Challenges in measuring aerosol cloud-mediated radiative forcing. Eos 2024;105. http://dx.doi.org/10.1029/2024EO245012, Published on 29 February 2024.

[6] Dagan Guy, Yeheskel Netta, Williams Andrew IL. Radiative forcing from aerosol–cloud interactions enhanced by large-scale circulation adjustments. Nat Geosci 2023;16:1092–8. http://dx.doi.org/10.1038/s41561-023-01319-8.

[7] Sinclair Kenneth, van Diedenhoven Bastiaan, Cairns Brian, Alexandrov Mikhail, Moore Richard, Crosbie Ewan, Ziemba Luke. Polarimetric retrievals of cloud droplet number concentrations. Remote Sens Environ 2019;228:227–40. http://dx.doi.org/10.1016/j.rse.2019.04.008, URL https://www.sciencedirect.com/science/article/pii/S0034425719301452.

[8] Wang Hengqi, Peng Yiran, Di Noia Antonio, Shang Huazhe, Letu Husi, van Diedenhoven Bastiaan, Hasekamp Otto P, Liu Yangang, Quaas Johannes. Global quantification of the dispersion effect with POLDER satellite data. Nat Commun 2025;16:7087. http://dx.doi.org/10.1038/s41467-025-62238-3.

[9] Nakajima Teruyuki, King Michael D. Determination of the optical thickness and effective particle radius of clouds from reflected solar radiation measurements. I - Theory. J Atmos Sci 1990;47:1878–93. http://dx.doi.org/10.1175/1520-0469(1990)047<1878:DOTOTA>2.0.CO;2.

[10] King Michael D, Tsay Si-Chee, Platnick Steven E, Wang Menghua, Liou Kuo-Nan. Cloud retrieval algorithms for MODIS: Optical thickness, effective particle radius, and thermodynamic phase. MODIS Algorithm Theor Basis Doc 1997;1997:440.

[11] Fu D, Di Girolamo L, Rauber RM, McFarquhar GM, Nesbitt SW, Loveridge J, Hong Y, van Diedenhoven B, Cairns B, Alexandrov MD, Lawson P, Woods S, Tanelli S, Schmidt S, Hostetler C, Scarino AJ. An evaluation of the liquid cloud droplet effective radius derived from MODIS, airborne remote sensing, and in situ measurements from CAMP^{2}Ex. Atmospheric Chem Phys 2022;22(12):8259–85. http://dx.doi.org/10.5194/acp-22-8259-2022, URL https://acp.copernicus.org/articles/22/8259/2022/.

[12] Kuji Makoto, Hayasaka Tadahiro, Kikuchi Nobuyuki, Nakajima Teruyuki, Tanaka Masayuki. The retrieval of effective particle radius and liquid water path of low-level marine clouds from NOAA AVHRR data. J. Appl Meteorol. 2000;39(7):999–1016. http://dx.doi.org/10.1175/1520-0450(2000)039<0999:TROEPR>2.0.CO;2, URL https://journals.ametsoc.org/view/journals/apme/39/7/1520-0450_2000_039_0999_troepr_2.0.co_2.xml.

[13] Rosenfeld D, Liu G, Yu X, Zhu Y, Dai J, Xu X, Yue Z. High-resolution (375 m) cloud microstructure as seen from the NPP/VIIRS satellite imager. Atmospheric Chem Phys 2014;14(5):2479–96. http://dx.doi.org/10.5194/acp-14-2479-2014, URL https://acp.copernicus.org/articles/14/2479/2014/.

[14] Zhang Zhibo, Platnick Steven. An assessment of differences between cloud effective particle radius retrievals for marine water clouds from three MODIS spectral bands. J Geophys Res: Atmospheres 2011;116(D20). http://dx.doi.org/10.1029/2011JD016216, URL https://agupubs.onlinelibrary.wiley.com/doi/abs/10.1029/2011JD016216.

[15] Painemal David, Zuidema Paquita. Assessment of MODIS cloud effective radius and optical thickness retrievals over the southeast Pacific with VOCALS-REx in situ measurements. J Geophys Res: Atmospheres 2011;116(D24). http://dx.doi.org/10.1029/2011JD016155, URL https://agupubs.onlinelibrary.wiley.com/doi/abs/10.1029/2011JD016155.

[16] Zhang Zhibo, Ackerman Andrew S, Feingold Graham, Platnick Steven, Pincus Robert, Xue Huiwen. Effects of cloud horizontal inhomogeneity and drizzle on remote sensing of cloud droplet effective radius: Case studies based on large-eddy simulations. J Geophys Res: Atmospheres 2012;117(D19). http://dx.doi.org/10.1029/2012JD017655, URL https://agupubs.onlinelibrary.wiley.com/doi/abs/10.1029/2012JD017655.

[17] Cho Hyoun-Myoung, Zhang Zhibo, Meyer Kerry, Lebsock Matthew, Platnick Steven, Ackerman Andrew S, Di Girolamo Larry, C.-Labonnote Laurent, Cornet Céline, Riedi Jerome, Holz Robert E. Frequency and causes of failed MODIS cloud property retrievals for liquid phase clouds over global oceans. J Geophys Res: Atmospheres 2015;120(9):4132–54. http://dx.doi.org/10.1002/2015JD023161, URL https://agupubs.onlinelibrary.wiley.com/doi/abs/10.1002/2015JD023161.

[18] Miller DJ, Zhang Z, Platnick S, Ackerman AS, Werner F, Cornet C, Knobelspiesse K. Comparisons of bispectral and polarimetric retrievals of marine boundary layer cloud microphysics: case studies using a LES–satellite retrieval simulator. Atmospheric Meas Tech 2018;11(6):3689–715. http://dx.doi.org/10.5194/amt-11-3689-2018, URL https://amt.copernicus.org/articles/11/3689/2018/.

[19] Gryspeerdt Edward, Quaas Johannes, Ferrachat Sylvaine, Gettelman Andrew, Ghan Steven, Lohmann Ulrike, Morrison Hugh, Neubauer David, Partridge Daniel, Stier Philip, Takemura Toshihiko, Wang Hailong, Wang Minghuai, Zhang Kai. Constraining the instantaneous aerosol influence on cloud albedo.

Proc Natl Acad Sci 2017;114:201617765. http://dx.doi.org/10.1073/pnas.1617765114.

[20] Hasekamp Otto, Gryspeerdt Edward, Quaas Johannes. Analysis of polarimetric satellite measurements suggests stronger cooling due to aerosol-cloud interactions. Nat Commun 2019;10:5405. http://dx.doi.org/10.1038/s41467-019-13372-2.

[21] Quaas Johannes, Arola Antti, Cairns Brian, Christensen Matt, Deneke Hartwig, Ekman A, Feingold Graham, Fridlind Ann, Gryspeerdt Edward, Hasekamp Otto, Li Zhanqing, Lipponen Antti, Ma Po-Lun, Mülmenstädt Johannes, Nenes Athanasios, Penner Joyce, Rosenfeld Daniel, Schrödner R, Sinclair Kenneth, Wendisch Manfred. Constraining the Twomey effect from satellite observations: issues and perspectives. Atmospheric Chem Phys 2020;20:15079–99. http://dx.doi.org/10.5194/acp-20-15079-2020.

[22] Jia H, Quaas J, Gryspeerdt E, Böhm C, Sourdeval O. Addressing the difficulties in quantifying droplet number response to aerosol from satellite observations. Atmospheric Chem Phys 2022;22(11):7353–72. http://dx.doi.org/10.5194/acp-22-7353-2022, URL https://acp.copernicus.org/articles/22/7353/2022/.

[23] Alexandrov Mikhail D, Cairns Brian, Emde Claudia, Ackerman Andrew S, van Diedenhoven Bastiaan. Accuracy assessments of cloud droplet size retrievals from polarized reflectance measurements by the research scanning polarimeter. Remote Sens Environ 2012;125:92–111. http://dx.doi.org/10.1016/j.rse.2012.07.012, URL https://www.sciencedirect.com/science/article/pii/S0034425712002866.

[24] Alexandrov Mikhail D, Cairns Brian, Wasilewski Andrzej P, Ackerman Andrew S, McGill Matthew J, Yorks John E, Hlavka Dennis L, Platnick Steven E, Thomas Arnold G, van Diedenhoven Bastiaan, Chowdhary Jacek, Ottaviani Matteo, Knobelspiesse Kirk D. Liquid water cloud properties during the polarimeter definition experiment (PODEX). Remote Sens Environ 2015;169:20–36. http://dx.doi.org/10.1016/j.rse.2015.07.029, URL https://www.sciencedirect.com/science/article/pii/S0034425715300870.

[25] Pörtge V, Kölling T, Weber A, Volkmer L, Emde C, Zinner T, Forster L, Mayer B. High-spatial-resolution retrieval of cloud droplet size distribution from polarized observations of the cloudbow. Atmospheric Meas Tech 2023;16(3):645–67. http://dx.doi.org/10.5194/amt-16-645-2023, URL https://amt.copernicus.org/articles/16/645/2023/.

[26] Buriez JC, Vanbauce C, Parol F, Goloub P, Herman M, Bonnel B, Fouquart Y, Couvert P, and G Seze. Cloud detection and derivation of cloud properties from POLDER. Int J Remote Sens 1997;18(13):2785–813. http://dx.doi.org/10.1080/014311697217332.

[27] Bréon François-Marie, Doutriaux-Boucher Marie. A comparison of cloud droplet radii measured from space. IEEE Trans Geosci Remote Sens 2005;43(8):1796–805. http://dx.doi.org/10.1109/TGRS.2005.852838, URL https://www.scopus.com/inward/record.uri?eid=2-s2.0-24944433458&doi=10.1109%2fTGRS.2005.852838&partnerID=40&md5=d8bcd10f103f5c883a44da4df8f40566 Cited by: 88.

[28] Di Noia A, Hasekamp OP, van Diedenhoven B, Zhang Z. Retrieval of liquid water cloud properties from POLDER-3 measurements using a neural network ensemble approach. Atmospheric Meas Tech 2019;12(3):1697–716. http://dx.doi.org/10.5194/amt-12-1697-2019, URL https://amt.copernicus.org/articles/12/1697/2019/.

[29] Werdell P, Behrenfeld Michael, Bontempi Paula, Boss Emmanuel, Cairns Brian, Davis Gary, Franz Bryan, Gliese Ulrik, Gorman Eric, Hasekamp Otto, Knobelspiesse K, Mannino Antonio, Martins Vanderlei, Mcclain Charles, Meister Gerhard, Remer Lorraine. The Plankton, Aerosol, Cloud, ocean Ecosystem (PACE) mission: Status, science, advances. Bull Am Meteorol Soc 2019;100. http://dx.doi.org/10.1175/BAMS-D-18-0056.1.

[30] Hasekamp Otto, Fu Guangliang, Rusli Stephanie, Wu Lianghai, Di Noia Antonio, Brugh Joost, Landgraf Jochen, Smit Martijn, Rietjens Jeroen, Amerongen Aaldert. Aerosol measurements by SPEXone on the NASA PACE mission: expected retrieval capabilities. J Quant Spectrosc Radiat Transfer 2019;227. http://dx.doi.org/10.1016/j.jqsrt.2019.02.006.

[31] Fu G, Rietjens J, Laasner R, van der Schaaf L, van Hees R, Yuan Z, et al. Aerosol retrievals from SPEXone on the NASA PACE mission: First results and validation. Geophys Res Lett 2025. http://dx.doi.org/10.1029/2024GL113525.

[32] Di Noia Antonio, Hasekamp Otto, Harten Gerard, Rietjens Jeroen, Smit Martijn, Snik F, Henzing Bas, Boer Júlia, Keller Christoph, Volten H. Use of neural networks in ground-based aerosol retrievals from multi-angle spectropolarimetric observations. Atmospheric Meas Tech 2015;8:281–99. http://dx.doi.org/10.5194/amt-8-281-2015.

[33] Di Noia Antonio, Hasekamp Otto, Wu Lianghai, van Diedenhoven Bastiaan, Cairns Brian, Yorks J. Combined neural network/Phillips-Tikhonov approach to aerosol retrievals over land from the NASA Research Scanning Polarimeter. Atmospheric Meas Tech 2017;10:4235–52. http://dx.doi.org/10.5194/amt-10-4235-2017.

[34] Gao Meng, Franz Bryan, Knobelspiesse K, Zhai Phil, Martins Vanderlei, Burton Sharon, Cairns Brian, Ferrare Richard, Gales Joel, Hasekamp Otto, Hu Yongxiang, Ibrahim Amir, McBride Brent, Puthukkudy Anin, Werdell P, Xu Xiaoguang. Efficient multi-angle polarimetric inversion of aerosols and ocean color powered by a deep neural network forward model. 2021, http://dx.doi.org/10.5194/amt-2020-507.

[35] Gao Meng, Knobelspiesse Kirk, Franz Bryan A, Zhai Peng-Wang, Martins Vanderlei, Burton Sharon P, Cairns Brian, Ferrare Richard, Fenn Marta A, Hasekamp Otto, Hu Yongxiang, Ibrahim Amir, Sayer Andrew M, Werdell P Jeremy, Xu Xiaoguang. Adaptive data screening for multi-angle polarimetric aerosol and ocean color remote sensing accelerated by deep learning. Front Remote Sens 2021;2. http://dx.doi.org/10.3389/frsen.2021.757832, URL https://www.frontiersin.org/articles/10.3389/frsen.2021.757832.

[36] Yuan Z, Fu G, Lin HX, Erisman JW, Hasekamp OP. Above cloud aerosol detection and retrieval from multi-angular polarimetric satellite measurements in a neural network ensemble approach. EGUsphere 2025;2025:1–23. http://dx.doi.org/10.5194/egusphere-2025-1488, URL https://egusphere.copernicus.org/preprints/2025/egusphere-2025-1488/.

[37] Hansen LK, Salamon Peter. Neural network ensembles. IEEE Trans Pattern Anal Mach Intell 1990;12:993–1001. http://dx.doi.org/10.1109/34.58871.

[38] Bishop Christopher. Training with noise is equivalent to Tikhonov regularization. Neural Comput 1995;7. http://dx.doi.org/10.1162/neco.1995.7.1.108.

[39] Rumelhart David, Hinton Geoffrey, Williams Ronald. Learning representations by back-propagating errors. Nature 1986;323(6088):533–6. http://dx.doi.org/10.1038/323533a0.

[40] Liu Liyuan, Jiang Haoming, He Pengcheng, Chen Weizhu, Liu Xiaodong, Gao Jianfeng, Han Jiawei. On the variance of the adaptive learning rate and beyond. In: Proceedings of the eighth international conference on learning representations. ICLR 2020, 2020.

[41] Kingma Diederik, Ba Jimmy. Adam: A method for stochastic optimization. In: International conference on learning representations. 2014.

[42] Yuan Z, Fu G, van Diedenhoven B, Lin HX, Erisman JW, Hasekamp OP. Cloud detection from multi-angular polarimetric satellite measurements using a neural network ensemble approach. Atmospheric Meas Tech 2024;17(9):2595–610. http://dx.doi.org/10.5194/amt-17-2595-2024, URL https://amt.copernicus.org/articles/17/2595/2024/.

[43] Hasekamp Otto, Landgraf J. A linearized vector radiative transfer model for atmospheric trace gas retrieval. J Quant Spectrosc Radiat Transfer 2002;75:221–38. http://dx.doi.org/10.1016/S0022-4073(01)00247-3.

[44] Hasekamp Otto, Landgraf Jochen. Linearization of vector radiative transfer with respect to aerosol properties and its use in satellite remote sensing. J Geophys Res 2005;110. http://dx.doi.org/10.1029/2004JD005260.

[45] Schepers D, Brugh J, Hahne Ph, Butz André, Hasekamp Otto, Landgraf J. LINTRAN v2.0: A linearised vector radiative transfer model for efficient simulation of satellite-born nadir-viewing reflection measurements of cloudy atmospheres. J Quant Spectrosc Radiat Transfer 2014;149:347–59. http://dx.doi.org/10.1016/j.jqsrt.2014.08.019.

[46] Hasekamp Otto, Litvinov Pavel, Butz André. Aerosol properties over the ocean from PARASOL multi-angle photopolarimetric measurements. J Geophys Res 2011;116:D14204. http://dx.doi.org/10.1029/2010JD015469.

[47] Fu Guangliang, Hasekamp Otto. Retrieval of aerosol microphysical and optical properties over land using a multimode approach. Atmospheric Meas Tech 2018;11:6627–50. http://dx.doi.org/10.5194/amt-11-6627-2018.

[48] Fu Guangliang, Hasekamp Otto, Rietjens Jeroen, Smit Martijn, Di Noia Antonio, Cairns Brian, Wasilewski Andrzej, Diner David, Seidel Felix, Xu Feng, Knobelspiesse K, Gao Meng, Da Silva Arlindo, Burton Sharon, Hostetler Chris, Hair John, Ferrare Richard. Aerosol retrievals from different polarimeters during the ACEPOL campaign using a common retrieval algorithm. Atmospheric Meas Tech 2020;13:553–73. http://dx.doi.org/10.5194/amt-13-553-2020.

[49] Lu Sha, Landgraf Jochen, Fu Guangliang, van Diedenhoven Bastiaan, Wu Lianghai, Rusli Stephanie, Hasekamp Otto. Simultaneous retrieval of trace gases, aerosols, and cirrus using RemoTAP—The global orbit ensemble study for the CO2M mission. Front Remote Sens 2022;3:914378. http://dx.doi.org/10.3389/frsen.2022.914378.

[50] de Rooij WA, van der Stap CCAH. Expansion of Mie scattering matrices in generalized spherical functions. Astron Astrophys 1984;131(2):237–48.

[51] Hess Michael, Koepke Peter, Schult I. Optical properties of aerosols and clouds: The software package OPAC. Bull Am Meteorol Soc 1998;79:831–44. http://dx.doi.org/10.1175/1520-0477(1998)079<0831:OPOAAC>2.0.CO;2.

[52] van Diedenhoven Bastiaan, Ackerman Andrew S, Fridlind Ann M, Cairns Brian, Riedi Jerome. Global statistics of ice microphysical and optical properties at tops of optically thick ice clouds. J Geophys Res: Atmospheres 2020;125:e2019JD031811. http://dx.doi.org/10.1029/2019JD031811.

[53] Dubovik Oleg, Sinyuk Alexander, Lapyonok Tatyana, Holben Brent N, Mishchenko Michael, Yang Ping, Eck Tom F, Volten Hester, Muñoz Olga, Veihelmann Ben, van der Zande Wim J, Leon Jean-Francois, Sorokin Michael, Slutsker Ilya. Application of spheroid models to account for aerosol particle nonsphericity in remote sensing of desert dust. J Geophys Res 2006;111:D11208. http://dx.doi.org/10.1029/2005JD006619.

[54] Wanner Wolfgang, Li Xiaowen, Strahler Alan H. On the derivation of kernels for kernel-driven models of bidirectional reflectance. J Geophys Res: Atmospheres 1995;100(D10):21077–89. http://dx.doi.org/10.1029/95JD02371.

[55] Litvinov Pavel, Hasekamp Otto, Cairns Brian. Models for surface reflection of radiance and polarized radiance: Comparison with airborne multi-angle photopolarimetric measurements and implications for modeling top-of-atmosphere measurements. Remote Sens Environ 2011;115(2):781–92. http://dx.doi.org/10.1016/j.rse.2010.11.005, URL https://www.sciencedirect.com/science/article/pii/S003442571000324X.

[56] Maignan Fabienne, Breon Francois-Marie, Fédèle Emilie, Bouvier Marc. Polarized reflectances of natural surfaces: Spaceborne measurements and analytical modeling. Remote Sens Environ 2009;113:2642–50. http://dx.doi.org/10.1016/j.rse.2009.07.022.

[57] Fan Cheng, Fu Guangliang, Di Noia Antonio, Smit Martijn, Rietjens Jeroen, Ferrare Richard, Burton Sharon, Li Zhengqiang, Hasekamp Otto, Rietjens H, Nl J. Use of a neural network-based ocean body radiative transfer model for aerosol retrievals from multi-angle polarimetric measurements. Remote Sens 2019;11:19. http://dx.doi.org/10.3390/rs11232877.

[58] Cox Charles, Munk Walter. Measurement of the roughness of the sea surface from photographs of the sun's glitter. J Opt Soc Am 1954;44(11):838–50. http://dx.doi.org/10.1364/JOSA.44.000838, URL https://opg.optica.org/abstract.cfm?URI=josa-44-11-838.

[59] Hasekamp O, Litvinov P, Fu G, Chen C, Dubovik O. Algorithm evaluation for polarimetric remote sensing of atmospheric aerosols. Atmos. Meas Tech 2024;17:1497–525. http://dx.doi.org/10.5194/amt-17-1497-2024, data available at: https://public.spider.surfsara.nl/project/spexone/POLDER/GRIDDED/, last [Access 5 June 2022].

[60] Tilstra LG, Tuinder ONE, Wang P, Stammes P. Surface reflectivity climatologies from UV to NIR determined from earth observations by GOME-2 and SCIAMACHY. J Geophys Res: Atmospheres 2017;122(7):4084–111. http://dx.doi.org/10.1002/2016JD025940, URL https://agupubs.onlinelibrary.wiley.com/doi/abs/10.1002/2016JD025940.

[61] Mayer B, Hoch SW, Whiteman CD. Validating the MYSTIC three-dimensional radiative transfer model with observations from the complex topography of Arizona's Meteor Crater. Atmospheric Chem Phys 2010;10(18):8685–96. http://dx.doi.org/10.5194/acp-10-8685-2010, URL https://acp.copernicus.org/articles/10/8685/2010/.

[62] Emde C, Pörtge V, Manev M, Mayer B. Retrieval of cloud fraction and optical thickness of liquid water clouds over the ocean from multi-angle polarization observations. Atmospheric Meas Tech 2024;17(23):6769–89. http://dx.doi.org/10.5194/amt-17-6769-2024, URL https://amt.copernicus.org/articles/17/6769/2024/.

[63] Miller Dan J. Satellite simulator studies of the impact of cloud inhomogeneity on passive cloud remote sensing retrievals (Ph.D. thesis), University of Maryland, Baltimore County; 2017, URL https://www.proquest.com/dissertations-theses/satellite-simulator-studies-impact-cloud/docview/1984625298/se-2 Order No. 10642202.